Accepted Manuscript

C-REDOR curves of extended spin systems

Vinicius Ribeiro Celinski, Johannes Weber, Jörn Schmedt auf der Günne[a)]

Department Chemie, Ludwig-Maximilians-Universität München (LMU), Munich, D-81377, Germany

Keywords: NMR, heteronuclear recoupling, dipole-dipole interaction, Magic-Angle-Spinning, multiple-spin system, pulse sequence, solid-state

Abstract

The convergence of simulated C-REDOR curves of (infinitely) large spin systems is investigated with respect to the number of spins considered in the calculations. Taking a sufficiently large number of spins (> 20000 spins) into account enables the simulation of converged C-REDOR curves over the entire time period and not only the initial regime. The calculations are based on an existing approximation within first order average Hamiltonian theory (AHT), that assumes absence of homonuclear dipole-dipole interactions. The C-REDOR experiment generates an average Hamiltonian close to the idealized AHT behavior even for multiple spin systems including multiple homonuclear dipole-dipole interactions which is shown from numerically exact calculations of the spin dynamics. Experimentally it is shown that calculations accurately predict the full, experimental C-REDOR curves of the multi-spin systems ^{31}P-^{19}F in apatite, ^{31}P-^{1}H in potassium trimetaphosphimate and ^{1}H-^{31}P in potassium dihydrogen phosphate. We also present ^{13}C-^{1}H and ^{15}N-^{1}H data for the organic compounds glycine, L-alanine and L-histidine hydrochloride monohydrate which require consideration of molecular motion. Furthermore, we investigated the current limits of the method from systematic errors and we suggest a simple way to calculate errors for homogeneous and heterogeneous samples from experimental data.

[a)] Author to whom correspondence should be addressed. Electronic mail: gunnej@cup.uni-muenchen.de

1   Introduction

In solid-state NMR internuclear distances are often determined from experiments which selectively recouple the dipole-dipole interaction [1-4] under magic-angle spinning (MAS) conditions. An example is the measurement of through-space heteronuclear dipole-dipole couplings to obtain interatomic distance information [5-11]. Among the suitable recoupling sequences rotational echo double resonance (REDOR) [8] is one of the most prominent [12-19], since it is robust with respect to radio-frequency imperfections and able to recouple even small dipole-dipole couplings due to the refocussing π-pulse. REDOR-like pulse sequences have a number of applications, addressing structural aspects of glasses [20,21], polymers [22] and crystalline powders [23], from organic [24] and inorganic [25] bulk materials to nanoparticles [11,18], and ultimately biological samples [17,26].

For structural applications of REDOR experiments it is often necessary to calculate REDOR curves for large spin systems [15,18,27]. With conventional spin-density matrix based programs [28-30] the calculation can be very time consuming [31], because the manipulation of matrix representations leads to a strongly non-linear scaling behavior with respect to the number of spins. Depending on the program the simulation is thus limited to about 15 spins (I=1/2) [28-34]. While limited by the spin system size this approach has the advantage that it allows a rigorous treatment including terms from the chemical shift and the homonuclear dipole-dipole interaction.

A linear scaling behavior with respect to the spin system size can be achieved by shifting away from a numerically exact calculation of the REDOR curve to an approximation correct to first order average Hamiltonian theory (AHT) that takes only terms from the heteronuclear dipole-dipole interaction into account. Expressions for REDOR curves of multi-spin systems SI_n [19,27,35,36] are available, which assume the absence of homonuclear interactions and only require the isotopes and Cartesian coordinates of the nuclei as input. The oscillations in the REDOR curve for a two-spin case are correctly described and it has been pointed out that the REDOR curve of a multiple-spin system is sensitive not only to the number and magnitude of dipole-dipole coupling constants but also the relative orientation of different heteronuclear coupling tensors. Interestingly, this orientation dependence cannot be observed in the initial regime of the REDOR curve, which can be predicted from the sum of squared dipole-dipole couplings constants [13,14] alone. The latter feature allows for a rapid analysis of the REDOR curves of glasses and nano-particles. Furthermore, modified analytical expressions have been suggested for jump dynamics in the fast motional regime [27,35].

Unfortunately, REDOR recouples not only heteronuclear but also terms related to the homonuclear dipole-dipole interaction which strictly speaking means that the analytical expressions mentioned in the previous paragraph are valid only in the case of a 2-spin system. $^{13}C\{^{1}H\}$-REDOR simulations

of a 5-spin system in glycine demonstrate, that homonuclear interactions do disturb the experiment (see Supp. Info.). This problem was first solved by Chan and coworkers with the introduction of C-REDOR [37,38], which makes use of a symmetry based [2] rotor-synchronized pulse sequence of the type CN_n^v, that allows the suppression of unwanted contributions in the approximation up to first order average Hamiltonian theory [39-41]. To this end an appropriate choice of the symmetry numbers (N, n, v) and the basic C-element has to be made [37,38]. Following the same principle, other methods were developed that expand the scope of heteronuclear recoupling pulse sequences in multi-spin systems under MAS [41-44]. By application of symmetry-based sequences to two channels [45] it is even possible to achieve homonuclear decoupling on both channels while recoupling parts of the heteronuclear dipole-dipole interaction under high-resolution conditions. However these experiments are quite demanding with respect to the hardware and often unnecessary, because magic-angle spinning would average out the homonuclear interaction of non-isochronous spin-pairs anyway. It should be noted that none of these pulse-sequences decouples isotropic J-coupling which leads to small but non-commuting terms with the terms of the heteronuclear through space interaction [2].

A completely different approach was introduced with the HARDSHIP experiment [11] that takes advantage of the different $T_{2,H}$ relaxation times of protons in a nanoparticle shell and core. It is based on the approximation that long-ranged heteronuclear dipolar couplings commute with strong homonuclear dipolar couplings for short recoupling periods. Thus, it enables the measurement of weak heteronuclear dipolar interactions between abundant protons and an NMR-active nucleus and has been applied to the measurement of nanoparticle thickness.

In this contribution we combine the C-REDOR technique with a multiple-spin analysis on the basis of analytical formulas based on first order AHT (average Hamiltonian theory), which allows us to investigate whether it is feasible to use the complete REDOR curve of materials with abundant spins like ^{1}H, ^{31}P or ^{19}F for structural studies. To this end the extended spin systems found in crystalline model compounds need to be calculated, convergence with respect to the number of spins needs to be confirmed and implementations of analytical REDOR formulas for fast motional jump processes have to be validated against the experiment.

2   Experimental section

For efficient calculations of REDOR curves a Fortran95 program (compiled with gfortran, version 4.6.1) was written which allows for the calculation of REDOR curves to long time periods of abundant multi-spin systems. The program tests powder average convergences automatically and allows for jump dynamics according to eqs. 1-4. Lebedev [46] and ZCW [47-49] averaging schemes with 3-angle sets were used for powder averaging. Because the program is based on an analytical

description (section 3.1) it achieves close to linear scaling with respect to the number of spins in the spin system.

The SIMPSON package (version 2.0.0) was used to validate our program against numerically exact calculations of the evolution of the density-matrix [28,50]. Convergence with respect to the number of orientations in the powder averaging scheme and the time integration step-width was tested in every case.

The sample fluorapatite $Ca_5(PO_4)_3F$ is a natural mineral obtained from the town of Mapimí (Durango, Mexico). Potassium trimetaphosphimate ($K_3(PO_2NH)_3$) as synthesized in reference [51] was identified by x-ray diffraction [51,52]. Enriched $^{13}C_2$-glycine and ^{13}C-^{15}N-glycine (both 99% pure) were purchased from Eurisotop and potassium dihydrogen phosphate (KH_2PO_4) (99% pure) from Merck. Enriched $^{13}C_3$-^{15}N-L-alanine (99% pure) was purchased from Cambridge Isotope Laboratories. All samples were used without any further treatment.

Atom positions were extracted from the respective crystal structures (fluorapatite [53], KH_2PO_4 [54], glycine [55], L-alanine [56]) to calculate the dipole-dipole couplings constants and Euler angles $\Omega_{PC}= \{\alpha_{PC}, \beta_{PC}, \gamma_{PC}\}$ which relate principal axis to the crystal frame. For KH_2PO_4, glycine and alanine H-positions stem from neutron diffraction studies. For $K_3(PO_2NH)_3$ the hydrogen positions of the crystal structure [52] were refined by a quantum chemical structure optimization because of the lack of neutron diffraction data and because contradicting H-positions that can be found in literature [51,52]. The partial optimization was performed under periodic boundary conditions with the VASP program [57-60], version 4.6.28, using the projector augmented plain wave (PAW) method [61,62]. A Γ-centered k-point mesh [63] with four points in each direction (4x4x4) was used and the plane wave energy cutoff was set to 500 eV. The PBE density functional [64] was used with the standard pseudo potentials delivered for PBE/PAW with VASP. Optimizations were considered as converged when the energy between two subsequent steps was below 10^{-7} eV and the residual forces were converged to 10^{-6} eV/Å.

Solid State NMR experiments on fluorapatite were conducted at a magnetic field of 4.7 T on a Bruker Avance II-200 equipped with a 2.5 mm double resonance MAS probe at ^1H frequency of 200.175 MHz. Solid State NMR experiments on $K_3(PO_2NH)_3$, $^{13}C_2$-glycine, ^{13}C-^{15}N-glycine, $^{13}C_3$-^{15}N-L-alanine and KH_2PO_4 were conducted at a magnetic field of 11.7 T on a Bruker Avance III-500 spectrometer equipped with a 1.3 mm double resonance MAS probe at ^1H frequency of 500.13 MHz. Saturation combs were used before all repetition delays, to prevent unwanted coherence order transfer pathways from contributing to the observed signal.

The channels used in the C-REDOR experiments described below are denoted as S{I}, where S refers to the observed nucleus and I to the recoupled one. $^{19}F\{^{31}P\}$ experiments on fluorapatite were performed at a sample spinning frequency v_r of 20 kHz with a recycle delay set to 3 s and

accumulated 32 transients/FID. $^{31}P\{^1H\}$ experiments on $K_3(PO_2NH)_3$ were performed at a v_r of 50 kHz with a recycle delay set to 30 s and accumulated 16 transients/FID. $^1H\{^{31}P\}$ experiments on KH_2PO_4 were performed at a v_r of 50 kHz with a recycle delay set to 3 s and accumulated 16 transients/FID. $^{13}C\{^1H\}$ experiments on $^{13}C_2$-glycine were performed at a v_r of 50 kHz with a recycle delay set to 64 s and accumulated 16 transients/FID. $^{15}N\{^1H\}$ experiments on ^{13}C-^{15}N-glycine were performed at a v_r of 50 kHz with a recycle delay set to 4 s and accumulated 64 transients/FID. $^{15}N\{^1H\}$ experiments on $^{13}C_3$-^{15}N-L-alanine were performed at a v_r of 40 kHz with a recycle delay set to 10 s and accumulated 512 transients/FID. $^{13}C\{^1H\}$ experiments on $^{13}C_3$-^{15}N-L-alanine were performed at a v_r of 40 kHz with a recycle delay set to 98 s and accumulated 16 transients/FID. Coherence transfer pathway selection was achieved with a 16 step nested phase-cycle in all experiments.

Whenever the sample spinning frequencies v_r were higher than 40 kHz, a modified C-REDOR pulse sequence was used. It synchronizes the windowless C-REDOR sequence by merging the 180_0 pulse in the middle of the recoupled channel and the subsequent 90_0 pulse from the POST [65] scheme of the first C-element into a 90_{180} pulse as shown in Figure 1 (note the opposite phase). The idea is to bring one-spin magnetization to the same orientation in that part of the sequence, but only through a different path. In this manner we gain synchrony at the cost of breaking the internal symmetry of one of the C-elements. This *ansatz* may be found in literature [45]. C-REDOR curves were obtained using $POST-C2_2^1$, $POST-C3_3^1$, $POST-C4_4^1$ and $POST-C5_5^1$ as well as permutations thereof (also refered to as $POST-CX_x^1$ [37,38]), since they share the same first-order average Hamiltonian and their scaling factors are equal[37,38].

As a measure of the deviation between two C-REDOR data sets we use the root-mean-square deviation r [66]:

$$r = \sqrt{\frac{\sum(y_i(\text{data set1})-y_i(\text{data set2}))^2}{\sum y_i(\text{data set1})^2}} \tag{1}$$

We present r values between experimental (data set 1) and simulated (data set 2) data sets, as well as between two simulated data sets. Clearly, a comparison between two r values is only meaningful when the data sets from which they have been calculated feature an equal number of points m that run over the same time period.

In order to relate the isotropic chemical shift δ_{iso}, the chemical shift anisotropy (CSA) δ_{aniso} and the asymmetry parameter η_{CS} to the principal elements of the shift tensor $(\delta_{11}, \delta_{22}, \delta_{33})$ we use the following definitions[28]: $\delta_{iso} = \frac{1}{3}(\delta_{xx}+\delta_{yy}+\delta_{zz})$, $\delta_{aniso} = \delta_{zz}-\delta_{iso}$, and $\eta_{CS} = (\delta_{yy}-\delta_{xx})/\delta_{aniso}$,

where $\delta_{11}, \delta_{22}, \delta_{33}$ are ordered according to $|\delta_{zz} - \delta_{iso}| \geq |\delta_{xx} - \delta_{iso}| \geq |\delta_{yy} - \delta_{iso}|$. The frequencies v_{ref}, defined by certain reference materials [67], define 0 ppm for the above stated deshielding values of $\delta_{11}, \delta_{22}, \delta_{33}$ and δ_{iso}.
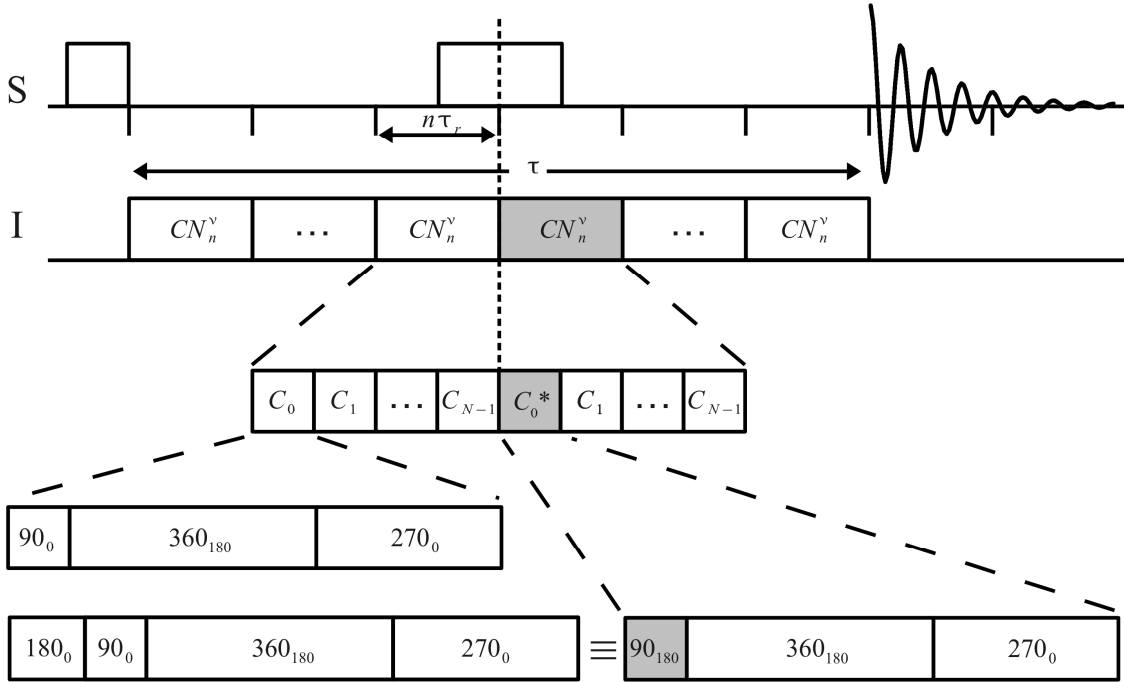
Figure 1: *Modified C-REDOR pulse sequence for the purpose of improved rotor synchronization; the rectangles on the S-channel represent the π/2- and π-pulses for the spin echo; the 180_0-pulse usually used in the middle of the sequence on the I-channel and the subsequent 90_0-pulse from the first C-element (C_0^*) are replaced by a single 90_{180}-pulse.*

3   Theory

3.1   Description of C-REDOR curves by analytical functions

In this section we shortly describe the analytical expressions for C-REDOR curves of multiple-spin systems (also with fast motional processes) which are based on REDOR articles by different authors [27,35], however slightly modified to allow for a general description of symmetry based pulse sequences.

In solid-state NMR it is usual to specify different frames of reference [2]:

$$\text{PAF} \xrightarrow[(\alpha_{PC},\ \beta_{PC},\ \gamma_{PC})]{} \text{CR} \xrightarrow[(\alpha_{CR},\ \beta_{CR},\ \gamma_{CR})]{} \text{ROT} \xrightarrow[(\alpha_{RL},\ \beta_{RL},\ \gamma_{RL})]{} \text{LAB}$$

where the Euler angles are defined according to the Rose convention [68]. The principal axis frame of dipolar interactions *PAF* has its z-axis along the vector connecting two spins and relates to the crystal frame *CRY* through the set of Euler angles α_{PC}, β_{PC} and γ_{PC}. Crystals and molecules have a fixed orientation to the z-axis of the rotor frame *ROT*, given by another set of Euler angles α_{CR}, β_{CR}

and γ_{CR}. Finally, the rotor frame *ROT* is connected to laboratory frame *LAB* (whose z-axis is along the magnetic field of the spectrometer) by the Euler angles α_{RL}, β_{RL} and γ_{RL}. Under MAS conditions these take the values $\alpha_{RL} = 2\pi\, v_r t + \alpha_0$, $\beta_{RL} \approx 54.74°$ and $\gamma_{RL} = 0$, where α_0 and γ_{RL} have no influence on the C-REDOR curve of a powder sample.

In a SI_n spin system, where *n* I-spins couple to an observed S-spin, the normalized dipolarly dephased signal S_D/S_0 of the C-REDOR experiment of a powder is a product of cosine terms as adopted from Brouwer [27], but modified to consider the magnitude of the scaling factor κ of the pulse sequence:

$$\left\langle \frac{S_D}{S_0} \right\rangle = \left\langle \prod_{k=1}^{n} \cos\left[\sqrt{2/3}\pi |\kappa| v_{dip,k}\ \tau \left(C_{1,k}\ \sin(\gamma_{CR}) - S_{1,k}\ \cos(\gamma_{CR}) \right) \right] \right\rangle \tag{2}$$

where $v_{dip,k}$ is the dipole coupling constant, defined as $v_{dip,k} = -\dfrac{\mu_0 \gamma_I \gamma_S \hbar}{8\pi^2 r_k^3}$, where γ_I and γ_S refer to the gyromagnetic ratios of the nuclei and r_k refers to the internuclear distance between spin S and the kth spin I. The dephasing time τ of the experiment (Figure 1) refers to the total amount of time during which the C-REDOR sequence is applied. The scaling factor κ is a complex number that reflects the efficiency of symmetry-allowed terms[41], which for C-REDOR CX_x^1 with a PostC element takes $|\kappa| \approx 0.24503$ [37]. The angle brackets indicate the powder average, that is performed by integrating over the Euler angles (α_{CR}, β_{CR}, γ_{CR}) that define the orientation of the dipolar interaction. The coefficients $C_{1,k}$ and $S_{1,k}$ depend solely on the orientation of the *k*-th interaction and are defined as [27,69]

$$\begin{aligned} C_{1,k} = 3\big(1 - 2\cos^2(\beta_{CR})\big)\sin(2\beta_{PC,k})\cos(\Gamma_k) \\ + 3\big(\sin^2(\beta_{PC,k})\cos(2\Gamma_k) - 3\cos^2(\beta_{PC,k}) + 1\big)\sin(\beta_{CR})\cos(\beta_{CR}) \end{aligned} \tag{3}$$

$$S_{1,k} = 3\big(\sin(2\beta_{PC,k})\sin(\Gamma_k)\cos(\beta_{CR}) - \sin^2(\beta_{PC,k})\sin(2\Gamma_k)\sin(\beta_{CR})\big) \tag{4}$$

where $\Gamma_k = \alpha_{CR} + \gamma_{PC,k}$.

Fast motional processes lead to a dynamic averaging and apparent reduction of the heteronuclear dipole-dipole couplings [70]. Fast motional processes can be for instance a rapidly rotating NH_3-group of an amino acid, which may be approximated by an infinitely fast jump process with *N* steps. Under fast motion of the recoupled spins, the dipolarly dephased signal of a powder yields a very similar expression to eq. (1) [27], again modified to consider the magnitude of the scaling factor κ of the pulse sequence:

$$\left\langle \frac{S_D}{S_0} \right\rangle = \left\langle \prod_{k=1}^{n} \cos\left[\sum_{j=1}^{N} p_{eq}(j)\left[\sqrt{2/3}\pi|\kappa|v_{dip,k}\tau\left(C_{1,k}\sin\gamma_{CR} - S_{1,k}\cos\gamma_{CR}\right)\right]\right]\right\rangle \tag{5}$$

where the cosine's argument is now the weighted sum of N possible positions of the k-th recoupled spin. The probability of a certain position is given by $p_{eq}(j)$, where $\sum_{j=1}^{N} p_{eq}(j) = 1$. While jump fast jump processes can be considered by this approach relaxational processes are not considered. In this sense the presented formula describe a way to simulate "relaxation-free" REDOR curves.

In order to generate REDOR curves, which for a given dipole-dipole coupling look the same regardless of which REDOR sequence was used, we use the universal dephasing time $\tau_{uds} = |\kappa|\tau$, [15,18] where $|\kappa|$ is the magnitude of the pulse-sequence dependent scaling factor of the recoupled heteronuclear dipole-dipole coupling term.

3.2 Statistical error analysis for homogeneous samples

For a routine error analysis of experimental REDOR curves it is necessary to distinguish different sources of errors. Various systematic errors (relating to the accuracy) are discussed in section 4.4 and estimates of the error margins for heterogeneous materials are suggested in section 3.3. In case of a homogeneous sample (this section) we suggest a simple statistical analysis based on error propagation which relates to the precision (but not the accuracy) of the points in the REDOR curve. Frequently, REDOR data are shown as the normalized difference between the reference signal S_0, alias full echo signal, and the dephased echo signal S_D. In order to avoid confusion with the error propagation treatment below, we define $R = \Delta S / S_0 = (S_0 - S_D)/S_0 = 1 - S_D/S_0$. In this formula ΔS means the difference $S_0 - S_D$.

Here we define a sample as being homogeneous, if its NMR peaks can be resolved and assigned to a specific site of its structure. For such cases, an error propagation [71] from the scatter of the experimental data points can be calculated. First, we fit the experimental data (S_0 data) of the reference experiment with a decaying exponential function, then we approximate the standard deviation ΔS_0 from the deviation of the experimental data points from the fitted curve. A statistical error ΔR of the normalized difference $\boldsymbol{R}$ can be approximated by error propagation:

$$\Delta R = \sqrt{\left(\frac{\partial R}{\partial S_0}\Delta S_0\right)^2 + \left(\frac{\partial R}{\partial S_D}\Delta S_D\right)^2} \tag{6}$$

where the Δ in expressions (5) and (6) convey an **error margin**. Assuming the standard deviation for the dephasing experiment ΔS_D is equal to the one of the reference experiment ΔS_0, the

statistical error is given by:

$$\Delta R = \sqrt{\left(\frac{S_D}{S_0^2} \Delta S_0 \right)^2 + \left(\frac{1}{S_0} \Delta S_0 \right)^2} \tag{7}$$

3.3 Error analysis for heterogeneous samples

It is possible that an NMR peak originates from spins that are located in different environments, but coincidentally feature the same chemical shift. This can be the case for amorphous materials or heterogeneous mixtures, for example as in the case of a nanoscale zinc phosphate [15] (Figure 2). REDOR simulations as described in section 3.1are only able to produce relaxation-free REDOR curves for such heterogeneous mixtures. Unlike the homogeneous case, the experimental, normalized intensity difference $\Delta S^{\mathrm{exp}} / S_0^{\mathrm{exp}} = \left(S_0^{\mathrm{exp}} - S_D^{\mathrm{exp}} \right) / S_0^{\mathrm{exp}}$ is no longer a good approximation for the relaxation-free REDOR curve, even when the experimental data are free of statistical errors and assuming that relaxational effects can be factorized in the same way for the $S_0^{\mathrm{exp}}(\tau)$ and the $S_D^{\mathrm{exp}}(\tau)$ curves (silently assumed below): consider for example a signal of two components, where the main component A features a very short T_2 value combined with a small heteronuclear dipole-dipole coupling constant while the minor component B has a long T_2 value combined with a big coupling constant. While the theoretically calculated REDOR curve would be a weighted superposition of the REDOR curves of the two components and thus looks similar to the curve of component A, the experimental curve plotted as the normalized intensity difference $\Delta S^{\mathrm{exp}} / S_0^{\mathrm{exp}} = \left(S_0^{\mathrm{exp}} - S_D^{\mathrm{exp}} \right) / S_0^{\mathrm{exp}}$ would look like the one of component B once the signal of component A has vanished by relaxation.

How can reliable error margins be estimated in this case? In the case of non-uniform relaxation over the sample we lose information about the cause/origin of the signal decay which is the difference between the full echo at $\tau = 0$s and the full echo at non-zero τ values. To calculate the upper and lower margins for $\Delta S^{\mathrm{exp}}(\tau) / S_0^{\mathrm{exp}}(\tau)$, we thus define $S_{blind}^{\mathrm{exp}}(\tau)$ as the difference between the maximum intensity S_{max}^{exp} at time $\tau = 0$s (dashed line in Figure 2) and the intensity of the fit curve $S_0^{\mathrm{exp}}(\tau)$ of the reference experiment at time τ (solid line in Figure 2). In simple cases the decay can be described with a decaying exponential with a single time constant.

$$S_{blind}^{\mathrm{exp}}(\tau) = S_{max}^{\mathrm{exp}} - S_0^{\mathrm{exp}}(\tau) \tag{8}$$

We distinguish two limiting cases with respect to a possible fast relaxing component which determines the REDOR behavior of S_{blind}^{exp}, in order to estimate what the relaxation-free, ideal

REDOR curve $\Delta S^{true} / S_0^{true} = \left(S_0^{true} - S_D^{true} \right) / S_0^{true}$ could look like in comparison to the experimental data:

Case 1 (upper margin): The "blind" echo intensity $S_{blind}^{exp}(\tau)$ refers to spins in the sample which have very strong heteronuclear dipolar couplings. Thus the relaxation-free dephased $S_D^{true}(\tau)$ and the relaxation-free full-echo intensity $S_0^{true}(\tau)$ become

$$S_D^{true}(\tau) = S_D^{exp}(\tau) \tag{9}$$

$$S_0^{true}(\tau) = S_{max}^{exp} = S_0^{exp}(\tau) + S_{blind}^{exp}(\tau) \tag{10}$$

for moderately small τ values. Consequently the maximum possible relaxation-free REDOR curve, i. e. the normalized difference $\Delta S^{true}(\tau) / S_0^{true}(\tau)$, could be calculated from the experimental data as follows.

$$\frac{\Delta S^{true}(\tau)}{S_0^{true}(\tau)} = \frac{S_{max}^{exp} - S_D^{exp}(\tau)}{S_{max}^{exp}} \tag{11}$$

which represents the dotted line in the example in Figure 2.

Case 2 (lower margin): The "blind" echo intensity $S_{blind}^{exp}(\tau)$ refers to spins in the sample which have no heteronuclear dipolar couplings and thus show no dephasing at all. Then the relaxation-free dephased $S_D^{true}(\tau)$ and the relaxation-free full echo intensity $S_0^{true}(\tau)$ becomes

$$S_D^{true}(\tau) = S_D^{exp}(\tau) + S_{blind}^{exp}(\tau) = S_D^{exp}(\tau) + S_{max}^{exp} - S_0^{exp}(\tau) \tag{12}$$

$$S_0^{true}(\tau) = S_{max}^{exp} = S_0^{exp}(\tau) + S_{blind}^{exp}(\tau). \tag{13}$$

Consequently the minimum possible relaxation-free REDOR curve, i.e. the normalized difference $\Delta S^{true}(\tau) / S_0^{true}(\tau)$, can be calculated from the experimental data as

$$\frac{\Delta S^{true}(\tau)}{S_0^{true}(\tau)} = \frac{S_0^{exp}(\tau) - S_D^{exp}(\tau)}{S_{max}^{exp}} \tag{14}$$

which is represented by the dashed dotted line in Figure 2.

Clearly, the true relaxation-free REDOR curve should be somewhere between these two limiting cases. In our experience the error margins determined in this way are large whenever the full-echo signal shows a fast decay.
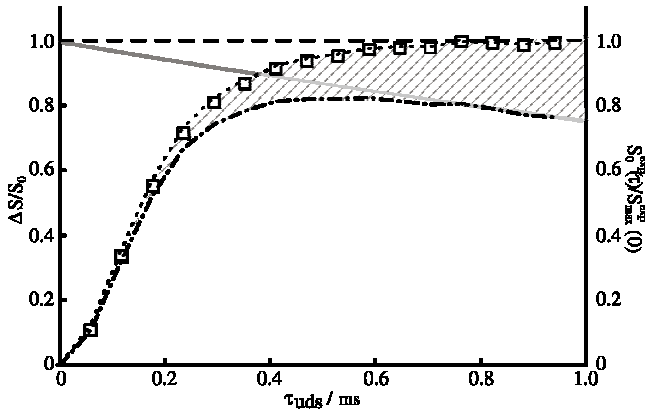
Figure 2: $^{31}P\{^{1}H\}$-C-REDOR curve of a nanoscale zinc phosphate [15] as an example for the error analysis of heterogeneous samples; experimental data (open squares) and upper (dotted, eq. 11) and lower (dashed dotted line, eq. 14) error margins share the axis on the left; the fitted full echo data ($S_0^{exp}(\tau)$ data, solid gray line) and the maximum signal S_{max}^{exp} extrapolated to time point 0 ms (dashed line) share the normalized axis on the right; hatching marks the region where the true relaxation-free REDOR curve can be found.

4   Results and Discussion

4.1   Validation by comparison to numerically exact calculations

Validation of the first order AHT expressions is necessary, if we want to simulate large spin systems. Therefore, we calculated the REDOR curve of a 10-spin system free of homonuclear dipole-dipole interactions according to eq. 2 and compared it with a fully converged, numerically exact simulation of the REDOR experiment of the same spin system (Figure 3). The calculation
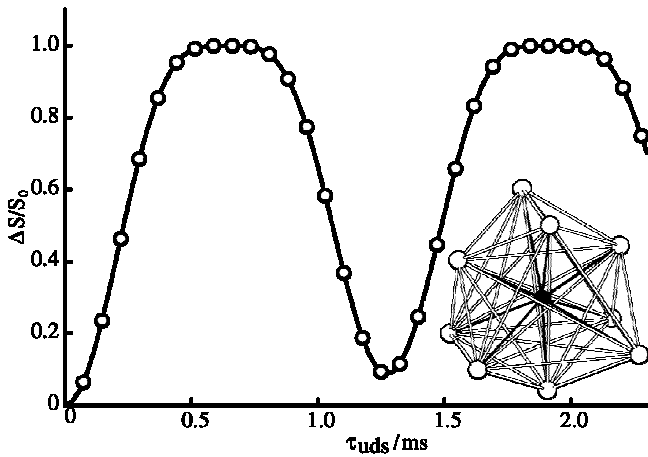
Figure 3: $^{19}F\{^{31}P\}$-REDOR curve of a 10 spin system for the validation of the first order AHT expression; open circles refer to a simulation using a numerically exact calculation of the spin-dynamics (SIMPSON) for a single orientation and the solid line was obtained by eq. 2; the inset shows the chosen spin system, a section from fluorapatite's crystal structure; white atoms represent phosphorus and the black atom fluorine; dipole-dipole interactions are shown as black (heteronuclear) and white (homonuclear) sticks.

refers to a small section of the crystal structure of fluorapatite [53], where one fluorine atom is

surrounded by nine phosphorus atoms. An illustration of the spin system with its dipole-dipole interactions is also depicted. We conclude that simple analytical first order AHT expressions are sufficient for the calculation of REDOR curves of bigger spin systems, which is in line with a previous study [72], which investigated the effect of "dipolar truncation" on REDOR curves for a pure heteronuclear Hamiltonian.

4.2   Convergence of large spin systems with respect to the number of Euler angle triplets

The dephased curves $S_D(\tau)$ of spin systems have the more zero-crossings the bigger the spin system is (eq. 2). It is thus not a priori clear how the convergence of a C-REDOR curve $R(\tau) = \Delta S(\tau)/S_0(\tau)$ with respect to the powder average depends on the number of recoupled spins n in the spin system. In case an increase of n would be accompanied by a need for an increased number of orientations n_{powder} of crystals in the powder averaging scheme to achieve convergence, the calculation of converged large spin systems could be prohibitive.

We define that the calculation of a C-REDOR curve $R(\tau)$ is converged if the root mean square deviation r (eq. 1) of two C-REDOR curves calculated with an increasing number of Euler angle triplets n_{powder} remains below a chosen convergence criterion σ. The numbers of Euler angle triplets n_{powder} for reasons of convenience were taken from lists of existing angle sets (Zaremba-Conroy-Wolfsburg (ZCW) scheme [47-49] $n_{powder} \in \{50,100,144,200,300,538,1154,3722,6044\}$, Lebedev scheme [46] $n_{powder} \in \{84,600,1980,4656,9060,15624,24780\}$) in the chosen powder angle scheme.
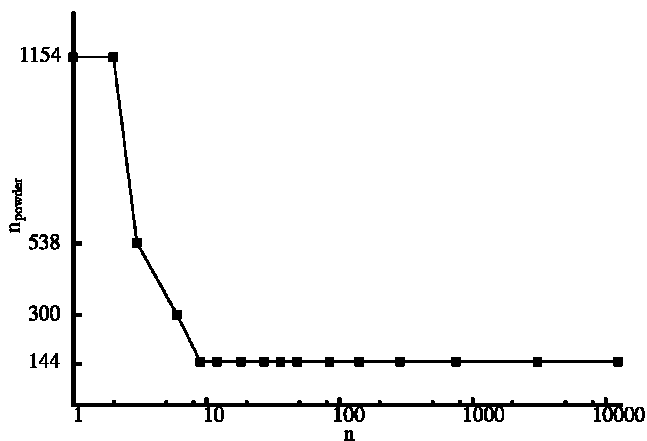
Figure 4: Number of Euler angle triplets n_{powder} (ZCW scheme) necessary for the calculation of converged $^{19}F\{^{31}P\}$-C-REDOR curves of fluorapatite as a function of the number n of recoupled spins (convergence criterion: $\sigma < 10^{-3}$).

$^{19}F\{^{31}P\}$ C-REDOR curves with different number of recoupled spins n were calculated (Figure 4) which were set up from sections of the crystal structure of apatite and a constant convergence

criterion $\sigma < 10^{-3}$. The necessary number of Euler angle triplets n_{powder} to achieve convergence as a function of the number of recoupled spins n starts at higher values and then steadily decreases so that in fact the calculation of converged C-REDOR curves of bigger spin systems requires fewer Euler angle triplets than that of very small spin systems. This dependence enables the calculation of converged C-REDOR curves of multiple-spin systems. The powder angle scheme based on the method by Zaremba [47], Conroy [48], and Wolfsberg [49] usually needed a smaller n_{powder} to reach convergence in this context than the schemes based on the Lebedev [46,73-75] method, except for $n = 1$.

4.3   C-REDOR analysis on crystalline model compounds

The crystalline model compounds were chosen as examples of abundant multi-spin systems, since the relevant NMR-active isotopes have close to or exactly 100% natural abundance. The crystal structures of the measured compounds are illustrated in Figure 5. The samples were chosen to reflect typical cases including static and dynamic spin systems, where the word "dynamic" refers to motional processes in solid matter, as for example rotations of methyl functions.

4.3.1   C-REDOR curves of static spin systems

In this section we validate calculated against experimental C-REDOR curves of $Ca_5(PO_4)_3F$, $K_3(PO_2NH)_3$ and KH_2PO_4. These have spin systems where fast motional processes can be neglected which refers for example to significant librational motion and jump dynamics.
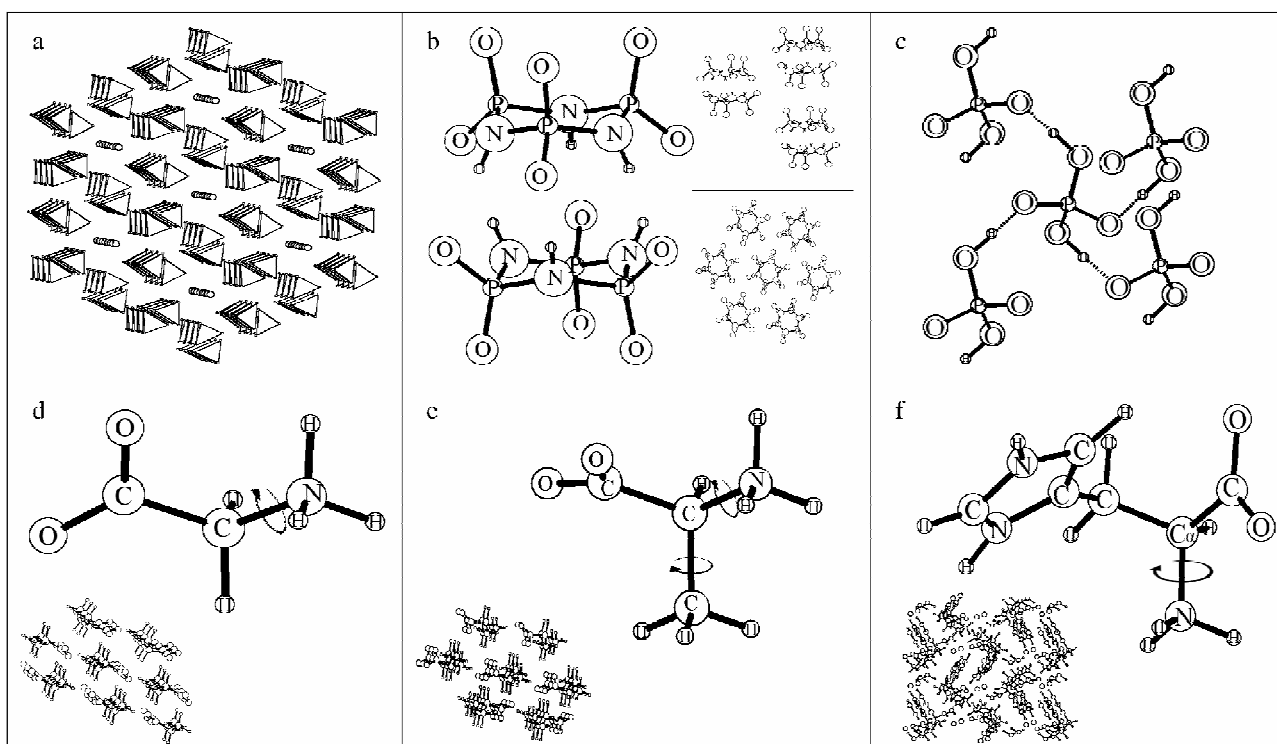
Figure 5: Crystal structures of the different reference compounds used in this article, to illustrate the spin-systems, rotational degrees of freedom and packing in the crystal structure: a) $Ca_5(PO_4)_3F$ (tetrahedrons correspond to PO_4^{3-}, circles to F^- ions), b) KH_2PO_4, c) $K_3(PO_2NH)_3$, d) glycine, e) L-alanine and f) L-histidine·HCl·H$_2$O; cations are not depicted; rotating groups in the zwitterionic amino acids are pointed out by an arrow.

$^{19}F\{^{31}P\}$-C-REDOR of $Ca_5(PO_4)_3F$

In the structure of fluorapatite (Figure 5a) "stacked" PO_4^--tetrahedra and lines of fluoride ions can be found. The P- and F-atoms occupy each one crystallographic orbit. A natural question to ask is how big the section of a crystal has to become to calculate a C-REDOR curve which is close to that of the infinite crystal lattice. Figure 6 depicts simulated $^{19}F\{^{31}P\}$-C-REDOR curves of spin systems

of different size and experimental data. Good agreement can be seen between experiment and simulation for the largest spin system ($n = 22147$). The calculation of a 4-spin system ($n = 3$) is clearly far from convergence with a $r = 0.176$ between experimental and simulated data sets. It reflects the first coordination sphere around the fluoride ion, consisting of three phosphorus atoms that are arranged in form of an equidistant coordination triangle. The 13-spin system simulation ($n = 12$) is already closer to convergence with $r = 0.032$. It comprises all phosphorus atoms surrounding the fluoride ion within a radius of 6 Å. Increasing the number of spins taken into account (not shown) eventually leads to a converged C-REDOR curve, which is reached in this case at the order of 80 spins with a $r = 0.020$ ($\sigma < 10^{-3}$). A similar result is obtained if we do not take the experimental data as reference but when we approximate the infinite spin system of an ideal crystal with a very large spin system ($n = 22147$) which accounts for heteronuclear dipole-couplings as small as $v_{dip} \approx -0.01 Hz$). With this noise-free data set as reference, convergence is reached at about 150 spins ($r < 10^{-3}$, not shown). We conclude that the calculation of large spin-
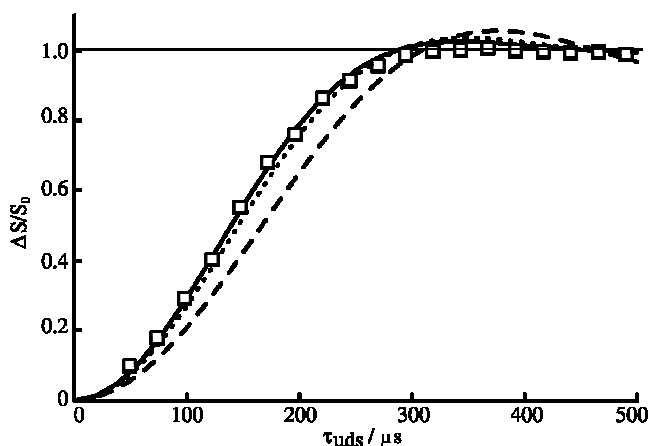
Figure 6: Experimental and simulated $^{19}F\{^{31}P\}$-C-REDOR data of fluorapatite; experimental data is represented by open squares, the lines represent fully converged simulations for spin systems of different sizes (n number of recoupled nuclei): n = 3 (dashed line, $r = 0.176$), n = 12 (dotted line, $r = 0.032$) and n = 22147 (solid line, $r = 0.019$); data was measured at a sample spinning frequency $v_r = 20$ kHz.

systems is required even for rather simple cases as for fluorapatite.

$^{31}P\{^1H\}$-C-REDOR of $K_3(PO_2NH)_3$

The crystal structure of $K_3(PO_2NH)_3$ is depicted in Figure 5b. Two trimetaphosphimate rings are linked by hydrogen bonds and stacked on one another forming columns. The P- and H-atoms occupy each one crystallographic orbit. The quantum chemically refined structure (see experimental part and CIF in Supp. Info.) was used to set up a big spin system ($n = 10692$). Again experiment and simulation (Figure 7) of $^{31}P\{^1H\}$-C-REDOR curves are in good agreement ($r = 0.025$).
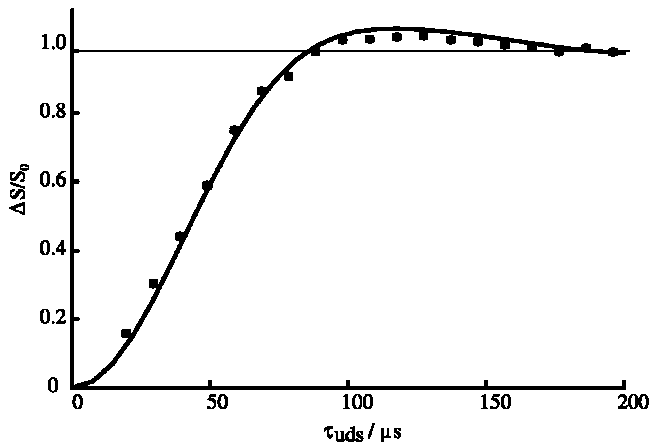
Figure 7: Experimental and simulated $^{31}P\{^1H\}$-C-REDOR curves ($r = 0.025$) of tripotassium trimetaphosphimate $K_3(PO_2NH)_3$; experimental data is represented by crosses along with error bars calculated using the derived expression for a homogeneous sample; the solid line represents the fully converged simulation ($n = 10692$); data was measured at $v_r =50$ kHz.

$^1H\{^{31}P\}$-C-REDOR of KH_2PO_4

Figure 5c shows the crystal structure of KH_2PO_4, where all corners of a PO_4^--tetrahedra are connected to other tetrahedra by a bridging hydrogen atom. The P- and H-atoms each occupy one crystallographic orbit. The simulation accounted for $n = 5610$ spins and with ($r = 0.037$) shows a fair agreement with experimental data (Figure 8).
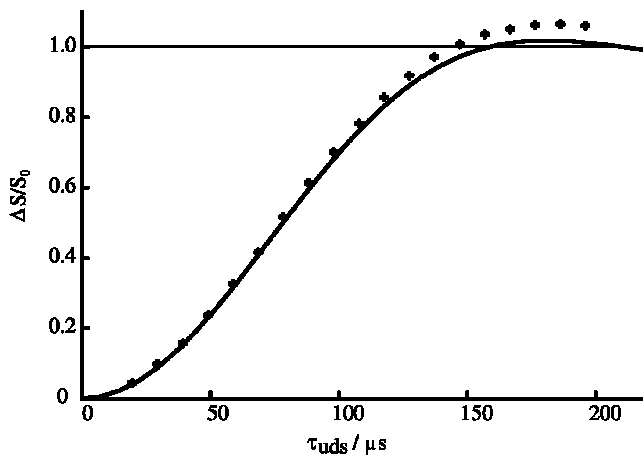
Figure 8: Experimental $^1H\{^{31}P\}$-C-REDOR and simulated $^1H\{^{31}P\}$-REDOR data ($r = 0.037$) of potassium dihydrogen phosphate; experimental data is represented by crosses along with error bars calculated using the derived expression for a homogeneous sample; the solid line represents the fully converged simulation ($n = 5610$); data was measured at $v_r =50$ kHz.

Overall, the reasonably good agreement between the previous three experiments and simulations confirms that C-REDOR curves can be calculated in the approximation described by eq. 2 and that consideration of a bigger number of spins is necessary to predict the C-REDOR curve from zero up to complete dephasing. However we do observe small but significant deviations outside the statistical limits which will be discussed below in section 4.4.

4.3.2 REDOR curves of dynamic spin systems

Glycine, L-alanine and L-histidine in L-histidine hydrochloride monohydrate are found as zwitterions in their crystalline states (Figure 5). Under normal conditions NH_3- and CH_3-groups rotate at high frequencies as compared to the NMR time scale []76. The effect of jump dynamics in the fast motional regime was calculated by taking into account the fast rotation of the NH_3-groups (in L-alanine also CH_3-group) according to eq. 4. Corresponding C-REDOR curves are drawn as dashed curves in the following figures. The solid curves simulate a low temperature case, where such rotations are frozen.

$^{13}C\{^1H\}$-C-REDOR of glycine and L-alanine

$^{13}C\{^1H\}$-C-REDOR curves were obtained for the carboxyl group in glycine and L-alanine (Figure 9) and the CH_3-group in L-alanine (Figure 10). C-REDOR curves of the $-CH_2-$ and $-CH-$ functions in L-alanine and glycine, respectively, were not considered because of strong dipole-dipole couplings between ^1H and ^{13}C in these groups and - correspondingly - a very rapid dephasing of the echo signal with too few points on the C-REDOR time scale for meaningful comparison with simulated curves. Qualitatively all experimental C-REDOR curves exhibit a much slower dephasing process than expected from the static crystal structure. Better agreement between experiment and simulation can be reached when jump dynamics are incorporated into the simulations, which describe the rotation of the NH_3 and the CH_3 group around the C-N and the C-C axis, respectively. In the case of the carboxyl group in glycine we calculated between experimental and simulation data sets $r = 0.092$ when accounting for dynamics and $r = 0.114$ for the static case (Figure 9). For the carboxyl group in L-alanine we calculated $r = 0.252$ when comparing experimental data and a
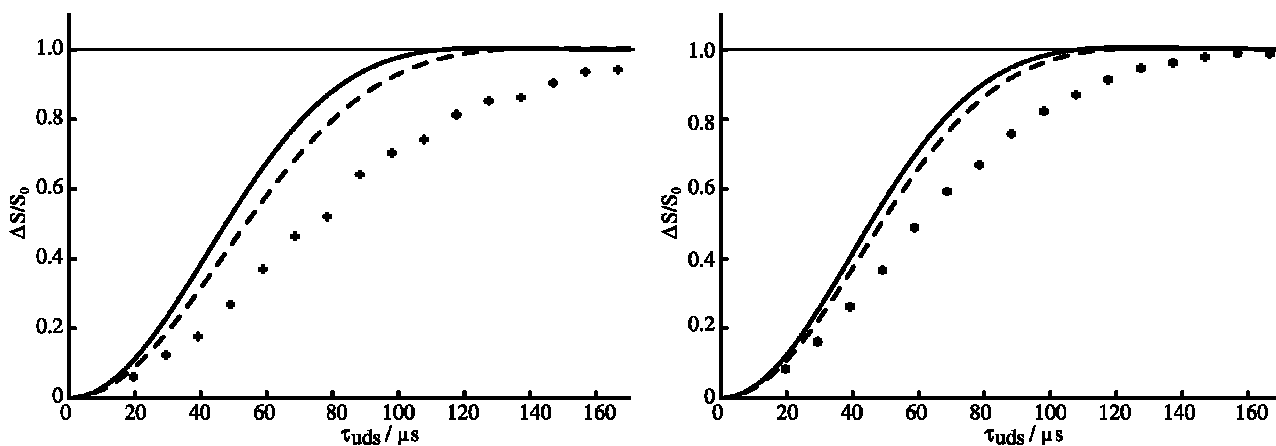
Figure 9: Experimental and simulated $^{13}C\{^1H\}$-C-REDOR data from the carboxyl group in L-alanine (left) and glycine (right); experimental data is represented by crosses along with error bars calculated using the derived expression for a homogeneous sample; fully converged simulation ($n = 2165$ for glycine and $n = 2405$ for L-alanine) of static case (solid) and under consideration of dynamics (dashed); data was measured at $v_r = 50$ kHz.

simulation with dynamics and $r = 0.332$ when comparing experiment with the static simulation. As expected the C-REDOR curve of the CH_3 function in L-alanine is far more sensitive to this dynamic correction (static: $r = 0.332$ and dynamic: $r = 0.104$) (Figure 10). The relative contribution of ^{13}C-^{1}H couplings which refer to static functional groups are bigger for the carboxyl function than for the CH_3 function in L-alanine which performs rapid rotational motion at room temperature. However
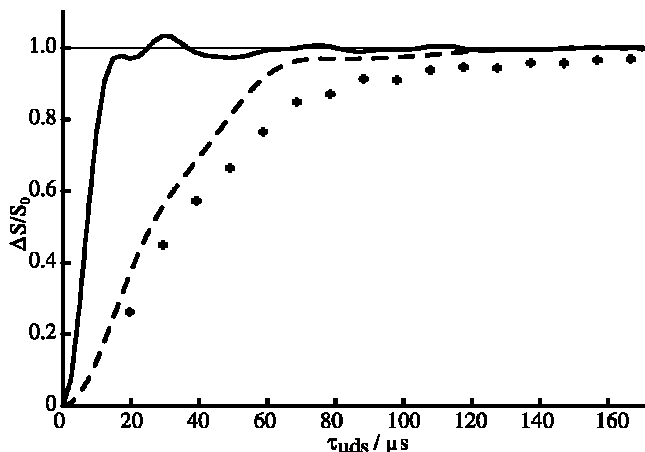
Figure 10: Experimental and simulated $^{13}C\{^{1}H\}$-C-REDOR data from the CH_3-group in L-alanine; experimental data is represented by crosses along with error bars calculated using the derived expression for a homogeneous sample; fully converged simulation ($n = 2405$) of static case (solid) and under consideration of dynamics (dotted); data was measured at $v_r = 50$ kHz.

the experimental curves (Figure 9 and 10) still show a slower dephasing than calculated for almost the complete REDOR curve.

$^{15}N\{^{1}H\}$-C-REDOR of glycine and L-alanine

The N-atoms in the zwitterionic crystal structures of glycine and L-alanine belong to NH_3 functions. As in the case of the CH_3 function in L-alanine, their rotation is thermally activated at room temperature and thus the respective C-REDOR curves (Figure 11) are better described with the dynamically corrected simulation ($r = 0.175$) than with the static description ($r = 0.612$). The shapes of the C-REDOR curve are well described over the complete time scale, while again faster dephasing of experimental data can be observed. Possible sources for these deviations will be discussed below.
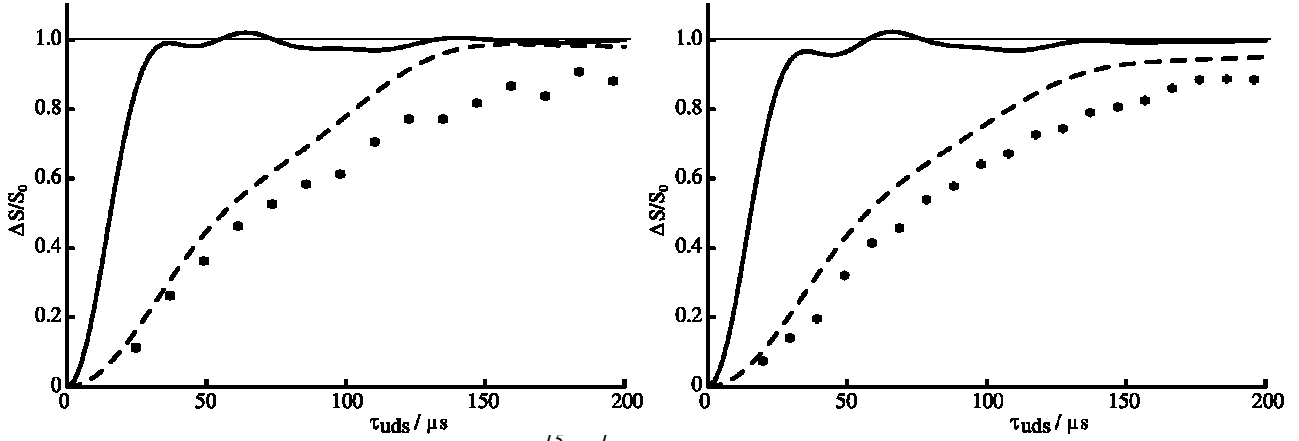
Figure 11: Experimental and simulated $^{15}N\{^1H\}$-C-REDOR data of L-alanine (left) and glycine (right); experimental data is represented by crosses along with error bars calculated using the derived expression for a homogeneous sample; fully converged simulation ($n = 2165$ for glycine and $n = 1461$ for L-alanine) of static case (solid) and under consideration of dynamics (dashed); data was measured at v_r =50 kHz (glycine) and v_r =40 kHz (L-alanine).

$^{13}C\{^1H\}$-C-REDOR of L-histidine hydrochloride monohydrate

From literature [77] we obtained a S-REDOR curve for the C_α function in L-histidine (Figure 12). Even though the data were obtained with a different REDOR sequence [77] a comparison with simulated data in the described simulation framework on the universal dephasing scale τ_{uds} is straight forward. The S-REDOR experiment is analogous to C-REDOR but uses RN_n^v - instead of CN_n^v -elements in order to suppress unwanted terms, for instance the dipole-dipole homonuclear interaction between spins of the I-channel. Here we calculated between experimental and simulation
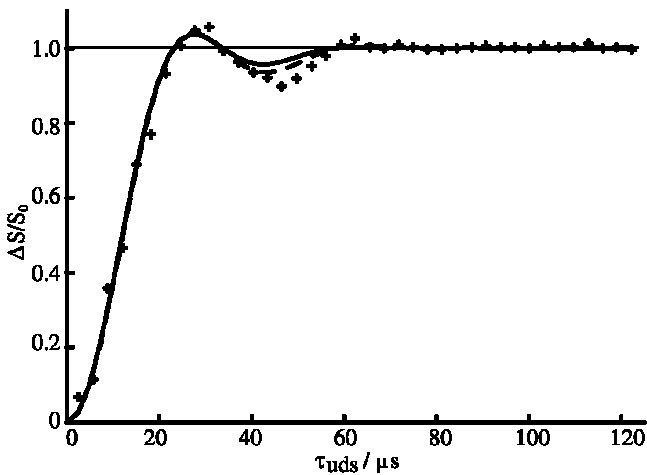
Figure 12: Experimental and simulated $^{13}C\{^1H\}$-S-REDOR [77] data from C_α in L-histidine hydrochloride monohydrate; experimental data is represented by crosses; fully converged simulation ($n = 1712$) of static case (solid) and under consideration of dynamics (dashed); data was measured at v_r =65 kHz.

data sets $r = 0.057$ when accounting for dynamics.

We conclude that disregarding motion is usually not justifiable for the calculation of REDOR curves of dynamic spin systems. In the case of L-histidine hydrochloride monohydrate the REDOR curve is dominated by the strong $^{13}C_\alpha$-^1H dipole-dipole coupling, so that the dynamics of the rotating NH_3-group play only a minor role. All other cases presented in this section showed an improved REDOR curve when dynamics were considered in the calculations, especially those relating to atoms within a rotating group (NH_3, CH_3). Despite the improvements when including dynamics, still more pronounced deviations were observed as compared to the curves of static systems.

4.4   Error discussion of REDOR curves

From the model study on crystalline compounds it becomes clear that despite the high-quality of the experimental data still significant deviations from the simulated curves are observed. In the following we want to discuss possible sources of errors which would have to be eliminated to reach still a better agreement between experiment and theory.

4.4.1   Statistical errors

For a statistical error analysis we differentiated between homogeneous and heterogeneous samples depending on whether there is a signal overlap on the spectrum or not. By assuming the same standard deviation for dephasing and reference experiments a propagation of the statistical error due to the noise in the spectrum can be calculated for the homogeneous case which applies to all samples in this contribution. For most of the presented experimental data the statistical error is so small, that the error bars can hardly be distinguished from data points in the figures. Clearly, noise does not explain the observed deviations.

4.4.2   Radio-frequency (rf) inhomogeneity, isotropic chemical shift, chemical shift anisotropy and anisotropic J-coupling

In order to investigate the effects of different interactions with numerically exact calculations, we chose the case of fluorapatite. We simulated 2-spin $^{19}F\{^{31}P\}$-C-REDOR curves using an effective dipole-dipole coupling constant [78] v_{eff} = -2063.87 Hz at v_{rot} = 20 kHz with varying parameters (see below).

Radio-frequency inhomogeneity is a direct consequence of the sample coil's geometry and signal amplitude errors can be of the order of 10% [79-81]. Even though radio-frequency inhomogeneity is suppressed to first order AHT in the C-REDOR experiment, its effects may still present due to higher order terms[2]. For this reason, we simulated C-REDOR curves where rf fields were

intentionally set to wrong values (Figure S3 in Supp. Info.). Close to the ideal pulse-nutation-frequency C-REDOR curves of two-spin systems change as if the dipole-dipole coupling is varied almost linearly. Hence nutation frequency errors can be treated as statistical errors including error propagation. A nutation frequency being too big by 3% leads to a too small dipole-dipole couplings constant by 4.8%. An error of of +5% leads to $r = 0.059$ between simulations with the intended and wrong rf field. This factor can explain small deviations in the experiment.

The POST element compensates for the symmetry-allowed isotropic chemical shifts in the C-REDOR experiment. We calculated r values between simulations with zero isotropic chemical shift and different offsets (Figure S4 in Supp. Info.). For a deviation of the same order as between experiment and converged simulation ($r = 0.019$, see section 4.3.1) one would need an offset of around 5 kHz ($r = 0.016$) on the recoupled channel, while an offset of 20 kHz would generate an r value about one order of magnitude higher ($r = 0.210$). Based on that and calculations at different v_r values (not shown) we conclude that offsets of the order of the sample spinning frequency v_r should be avoided, while offsets about 1/4 of the size of v_r should not be problematic.

A similar dependency is found for the dependency of C-REDOR curves on the chemical shift anisotropy δ_{aniso} of the recoupled I-spins (Figure S5 in Supp. Info.). Calculated r values between simulations with zero and varying δ_{aniso}-values serve as a measure for the strength of the dependency. Because the chemical shift scales with the external magnetic field it needs to be converted to frequency units for a fair comparison. While chemical shift anisotropies of $\delta_{aniso} \cdot v_{ref}$ of 6 kHz correspond to small deviations ($r = 0.021$, compare section 4.3.1) already values for $\delta_{aniso} \cdot v_{ref}$ of 16 kHz yield significant deviations ($r = 0.171$). Clearly, the dependence is less straight forward because it also depends on the relative orientations of the dipole-dipole interaction and the chemical shift tensor. However, simulations with random relative orientations between these interactions showed only an unsubstantial error ($r \approx 0.01$ for $\delta_{aniso} \cdot v_{ref} = 6$ kHz), that became more important at higher values ($r \approx 0.03$ for $\delta_{aniso} \cdot v_{ref} = 16$ kHz). Still as a rule of thumb, values which amount to about 1/4 of the sample spinning frequency v_r lead to tolerably small errors.

In the case of fluorapatite both the δ_{aniso}-values of ^{31}P and ^{19}F are known ($\delta_{aniso}\left(^{31}P\right) = 11.5$ppm [37], $\delta_{aniso}\left(^{19}F\right) = 56$ppm [82]). Converted to frequency units it is obvious why $^{31}P\{^{19}F\}$-C-REDOR experiments (not shown) in a field of 11.74 T show big deviations ($r = 0.46$, $v_r = 50$kHz) from the theoretical relaxation free C-REDOR curve while $^{19}F\{^{31}P\}$-C-REDOR experiments ($r = 0.019$, $v_r = 20$kHz, section 4.3.1) show almost perfect agreement. The values of $\delta_{aniso}\left(^{1}H\right)$ are around 10 ppm in glycine[83,84] and we assume similar or lower values for L-alanine with its additional CH_3

group [85], so that they shouldn't have any relevant influence under the chosen experimental conditions.

The anisotropic J-coupling J_{aniso} transforms as a second rank tensor with similar rotational properties as the through-space dipole-dipole coupling tensor. For that reason, the measurement of the dipole-dipole interactions with C-REDOR is always afflicted with a certain error, depending on the size of J_{aniso}. Fortunately, values for $^1J_{aniso}(^{13}C,^1H)$ and $^1J_{aniso}(^{15}N,^1H)$ [86] are usually small (<65 Hz) as compared to the dipole-dipole coupling constants. For this reason it may often be neglected as for the C-REDOR curves of the amino acids measured in this work. The one-bond isotropic J-couplings $^1J_{iso}(^{13}C,^1H)$ and $^1J_{iso}(^{15}N,^1H)$ are usually of the order of 150 Hz [87,88]. Simulations of C-REDOR curves taking these interactions into account showed nearly no deviations as compared to simulations where they were neglected ($r \approx 10^{-5}$). About 50 Hz [87] is the isotropic J-coupling $^1J_{iso}(^{13}C,^{13}C)$ between two ^{13}C nuclei as in isotopically labelled glycine. Such small values as compared to the size of the effective dipole-dipole coupling constant v_{eff} can hardly cause any change of calculated C-REDOR curves. Taking $^1J_{iso}(^{13}C,^{13}C) = 50 \text{ Hz}$ into consideration in the simulation of a 3-spin system as in glycine ($^{13}C_2$-^1H; $v_{CH,eff}$ = 6.4 kHz) induces a deviation of $r = 0.002$.

4.4.3   Hardware

Do pulse transients affect the performance of C-REDOR experiments? The transient-adapted POST-C7 sequence [89], for instance, has been shown to improve the transient-vulnerable POST-C7 sequence which uses the same C-element in a common commercial probe head. In order to investigate whether amplitude and phase transients of pulses influence the $POST - CX_x^1$ sequence, we estimated the quality-factor Q of our 1.3 mm probe head by measuring the transmission coefficient with a pickup coil near the sample coil. Probe heads with a high value of Q deliver a better signal-to-noise ratio at the cost of a slower recovery time of the tank circuit. Based on the approach used in [89] we then simulated a 2-spin system in the case of glycine with an effective dipole-dipole coupling constant v_{eff} of -6.4 kHz and $\delta_{aniso} \cdot v_{ref}$ of 2.5 kHz. The recovery time constant τ_R, which is directly proportional to Q was set to 0.5 µs, the offset-frequency $\omega_{eoff}/2\pi$ to 500 kHz and the integration time step to 20 ns. Calculations taking even higher values of τ_R into account than measured featured only negligible deviations. We can therefore rule out pulse-phase and amplitude transients as a source of the observed deviations.

The C-REDOR sequence demands a constant irradiation of one of the channels. High nutation frequencies are necessary at high spinning speeds over a relatively long time period, which in case

of our 1.3 mm MAS probe are applied through a solenoid coil with small wire diameter. For this reason, we investigated the stability of the probe head by comparing the amplitude of long pulses at the beginning and at their ends (up to 50 ms) at a ^{1}H nutation frequency of 100 kHz. No significant instability nor power droop could be observed ($< 1\%$), which excludes this factor as a possible error source.

4.4.4   Rotor synchronization

Rotor synchronization is desirable in experiments using symmetry-based sequences, because the π pulses can only refocus unwanted contributions to the Hamiltonian if these contributions cause exactly the same evolution before and after the π pulse. In REDOR like experiments this factor becomes more important the higher the sample spinning frequencies are, due to the finite length of the refocussing π pulse. A remedy to this problem may be using windowed sequences [44,90], given the free evolution of the spin system doesn't cause extra complications by non-commuting terms for example by strong homonuclear dipolar interactions. By breaking the internal symmetry of a basic element the scaling factor for the homonuclear dipole-dipole interaction can become a non-zero value. This means, the undesired homonuclear dipole-dipole interaction is reintroduced, as noticed by the ad hoc shortening of all pulse elements in a single C-cycle [43]. Similar to the approach used for SC14 [45], we achieve rotor synchronization at high sample spinning frequencies (> 40 kHz) by integrating the π pulse into the last part of the neighboring C-element (Figure 1). By affecting merely one pulse under the many pulses needed to select and suppress the desired interactions homonuclear effects should be of minor concern.

Sample spinning instabilities lead to pulse sequence asynchrony and can compromise the recoupling scheme especially at higher evolution times, where a complete dephasing may not be observed. Simulations of a 3-spin system based on the CH_2 fragment of glycine showed $r = 0.004$ between data sets recorded with the nominal sample frequency (50 kHz) and a deviation of 10 Hz. Therefore, we conclude small sample spinning instabilities do not affect the experiment substantially in the studied cases.

4.4.5   Homonuclear interactions

The effect of the homonuclear dipole-dipole interaction on C-REDOR curves was investigated for a 5-spin system (Figure S2 in Supp. Info.) $^{13}C_1$-$^1H_4$ oriented on the molecular structure of glycine, i.e. the $^{13}C_{carboxyl}$-$^1H_{2,CH2}$-$^1H_{2,NH3}$ which features strong ^{1}H-^{1}H dipole-dipole couplings of approximately -22 kHz. We calculated several data sets, namely $^{13}C\{^1H\}$-C-REDOR both with zero and full ^{1}H homonuclear dipole-dipole couplings which show only a minor increase of the r-value ($r = 0.017$). We conclude C-REDOR can effectively suppress homonuclear dipolar interactions under this

conditions, so that they do not act significantly on the experiment.

4.4.6 Scaling factor and relaxation

The good agreement between experiment and simulation for the C-REDOR curves of the static spin systems and the finding of deviations for dynamic spin systems outside the statistical limits of the experiment indicate that hardware issues and incomplete suppression of unwanted interactions as discussed in sections 4.4.2-4.4.5 are not responsible for the observed deviations. It is reassuring that we came to the same conclusions here, however for different reasons.

What wasn't discussed so far is the influence of relaxation. A simple approach to study the influence relaxation is to change the sample temperature to very low-temperatures, which would slow down T_2 relaxation and dynamics. In practice this turns out to be rather difficult if not impossible at sample spinning frequencies above 40 kHz which are often required for C-REDOR (see above). In fact in case of fast relaxation it is strictly speaking not correct to assume that the normalized difference $\Delta S/S_0$ is a good approximation for homogeneous samples for the relaxation-free model that is calculated. Take for example a spin on the recoupled channel which is subject to rapid T_1 relaxation. It would apparently reduce the heteronuclear dipolar interaction (self-decoupling [91]) and thus slow down the dephasing observed in the C-REDOR curve while the full-echo signal would remain untouched, so that the measured $\Delta S/S_0$ curve would not agree with the calculated relaxation-free curve.

We investigated this issue by obtaining C-REDOR curves with different C-elements, following the recipe $C_{\text{spoil-}X} = \left(90 + 180(\frac{X}{2}-1)\right)_0 - \left(360 \cdot \frac{X}{2}\right)_{180} - \left(270 + 180(\frac{X}{2}-1)\right)_0$, where $X \in Z_{even}$. The first element (X = 2) yields spoil-2, which corresponds to the PostC element. The next results are spoil-4 ($C_{\text{spoil-}4} = 270_0\text{-}720_{180}\text{-}450_0$), spoil-6 ($C_{\text{spoil-}6} = 450_0\text{-}1080_{180}\text{-}630_0$) and spoil-8 ($C_{\text{spoil-}8} = 630_0\text{-}1440_{180}\text{-}810_0$), with $|\kappa|$[41] 0.09801, 0.06301 and 0.04667, respectively. The latter are designed to spoil the scaling factor while selecting the same terms with respect to rank and order of the space and spin part in the average Hamiltonian, hence the name. It is worth noting the dependence of the required nutation frequency v_{nut} for the different elements spoil-X on the sample spinning frequency v_r, namely: $v_{nut} = Xv_r$. On the universal dephasing scale, which is independent from the scaling factor of the sequence, the experimental data should form a uniform curve given that relaxation is of no importance. In fact this wasn't the case (Figure S7 in Supp. Info.) and we observed that the C-REDOR curve of a sequence with a small scaling factor is influenced stronger by relaxation than that with a big scaling factor. Consistently, the observed C-REDOR curves are shifted to slower dephasing the smaller the scaling factor of the pulse sequence was (Figure S7 in

Supp. Info.). We conclude that relaxational processes are likely to be an important aspect for an improved analysis of C-REDOR curves in terms of structural and dynamical models.

5 Conclusion

In this contribution we investigated how well C-REDOR curves can be calculated as a function of the size of the spin system. In case of static spin systems, i. e. of materials where the nuclear positions are not subject to large amplitude motion and dynamics, we obtained excellent agreement between the experimental and simulated C-REDOR curves over the entire time period to complete dephasing. The simulated curves were obtained with a closed analytical formula which allows the calculation of spin systems with more than 20000 spins within a few hours on a common office PC. Such calculations may become helpful for imposing constraints for structure solution of crystalline powders by X-ray diffraction and for the analysis of nano-scale materials especially the localization of NMR active nuclei in the nano-scale morphology. We furthermore investigated how well the analytical approach is suited to predict C-REDOR curves for materials in which motion cannot be neglected on an atomic scale. While the calculated curve, which considered the rotation of a CH_3 or NH_3 function as a three-site jump, showed much better agreement with the experimental data there still are considerable deviations which indicate that an improved calculation of C-REDOR curves must be based on a more sophisticated treatment of motion and relaxation. Anyway, the suggested treatment based on analytical formula already allows a fast calculation of C-REDOR curves which may serve as boundary for the discussion of experimentally obtained curves and possibly these findings can be transferred to experiments with other REDOR like pulse sequences.

6 Associated content

In the supporting information there are calculated REDOR and C-REDOR curves and experimental C-REDOR curves with different C-elements (spoil-2, spoil-4) for the case of glycine as well as calculated C-REDOR curves with varying parameters for the case of fluorapatite. We also present the quantum chemically refined structure of tripotassium trimetaphosphimate ($K_3(PO_2NH)_3$) in a separate file (CIF).

7 Acknowledgments

[1] S. Dusold and A. Sebald, Annual Reports on NMR Spectroscopy **41**, 185–264 (2000).

[2] M.H. Levitt, Encyclopedia of NMR **9**, 165–196 (2002).

[3] K. Saalwächter and I. Schnell, Solid State Nucl. Magn. Reson. **22**, 154–187 (2002).

[4] H.W. Spiess, Encyclopedia of Magnetic Resonance 1–17 (2012).

[5] T.G. Oas, R.G. Griffin, and M.H. Levitt, J. Chem. Phys. **89**, 692–695 (1988).

[6] R. Fu, S.A. Smith, and G. Bodenhausen, Chem. Phys. Lett. **272**, 361–369 (1997).

[7] K. Saalwächter and K. Schmidt-Rohr, J. Magn. Reson. **145**, 161–172 (2000).

[8] T. Gullion and J. Schaefer, J. Magn. Reson. **81**, 196–200 (1989).

[9] C.P. Grey and A.J. Vega, J. Am. Chem. Soc. **117**, 8232–8242 (1995).

[10] T. Gullion, Chem. Phys. Lett. **246**, 325–330 (1995).

[11] K. Schmidt-Rohr, A. Rawal, and X.-W. Fang, J. Chem. Phys. **126**, 054701 (2007).

[12] C.A. Fyfe, A.R. Lewis, and J.M. Chézeau, Can. J. Chem. **77**, 1984–1993 (1999).

[13] M. Bertmer and H. Eckert, Solid State Nucl. Magn. Reson. **15**, 139–152 (1999).

[14] M. Bertmer, L. Züchner, J.C.C. Chan, and H. Eckert, Journal of Physical Chemistry B **104**, 6541–6553 (2000).

[15] M. Roming, C. Feldmann, Y.S. Avadhut, and J. Schmedt auf der Günne, Chem. Mater. **20**, 5787–5795 (2008).

[16] T. Gullion and A.J. Vega, Prog. Nucl. Magn. Reson. Spectrosc. **47**, 123–136 (2005).

[17] T. Gullion, Annu. Rep. NMR Spectrosc. 111–137 (2009).

[18] Y.S. Avadhut, J. Weber, E. Hammarberg, C. Feldmann, I. Schellenberg, R. Pöttgen, and J. Schmedt auf der Günne, Chem. Mater. **23**, 1526–1538 (2011).

[19] K. Nishimura, A. Naito, S. Tuzi, and H. Saito, J. Phys. Chem. B **103**, 8398–8404 (1999).

[20] H. Deters and H. Eckert, Solid State Nucl. Magn. Reson. **41**, 48–59 (2012).

[21] H. Eckert, Z. Phys. Chem. **224**, 1591–1653 (2010).

[22] S.S. Hou, F.L. Beyer, and K. Schmidt-Rohr, Solid State Nucl. Magn. Reson. **22**, 110–127 (2002).

[23] S.J. Sedlmaier, M. Döblinger, O. Oeckler, J. Weber, J. Schmedt auf der Günne, and W. Schnick, J. Am. Chem. Soc. **133**, 12069–12078 (2011).

[24] I. Hung, A.-C. Uldry, J. Becker-Baldus, A.L. Webber, A. Wong, M.E. Smith, S.A. Joyce, J.R. Yates, C.J. Pickard, R. Dupree, and S.P. Brown, J. Am. Chem. Soc. **131**, 1820–1834 (2009).

[25] P. Bertani, J. Raya, and J. Hirschinger, Solid State Nucl. Magn. Reson. **22**, 188–203 (2002).

[26] S.L. Grage and A. Watts, Annu. Rep. NMR Spectrosc. **60**, 191–228 (2006).

[27] E.B. Brouwer, R.D.M. Gougeon, J. Hirschinger, K.A. Udachin, R.K. Harris, and J.A. Ripmeester, Phys. Chem. Chem. Phys. **1**, 4043–4050 (1999).

[28] M. Bak, J.T. Rasmussen, and N.C. Nielsen, J. Magn. Reson. **147**, 296–330 (2000).

[29] M. Veshtort and R.G. Griffin, J. Magn. Reson. **178**, 248–282 (2006).

[30] P. Hodgkinson, pNMRsim: a General Simulation Program for Large Problems in Solid-state NMR (2011).

[31] P. Hodgkinson, D. Sakellariou, and L. Emsley, Chem. Phys. Lett. **326**, 515–522 (2000).

[32] V.E. Zorin, S.P. Brown, and P. Hodgkinson, J. Chem. Phys. **125**, 144508 (2006).

[33] P. Hodgkinson and L. Emsley, Prog. Nucl. Magn. Reson. Spectrosc. **36**, 201–239 (2000).

[34] M. Aluas, C. Tripon, J.M. Griffin, X. Filip, V. Ladizhansky, R.G. Griffin, S.P. Brown, and C. Filip, J. Magn. Reson. **199**, 173–187 (2009).

[35] J.M. Goetz and J. Schaefer, J. Magn. Reson. **127**, 147–154 (1997).

[36] C.A. Fyfe, A.R. Lewis, J.M. Chézeau, and H. Grondey, J. Am. Chem. Soc. **119**, 12210–12222 (1997).

[37] J.C.C. Chan and H. Eckert, J. Chem. Phys. **115**, 6095–6105 (2001).

[38] J.C.C. Chan, Chem. Phys. Lett. **335**, 289–297 (2001).

[39] Y.K. Lee, N.D. Kurur, M. Helmle, O.G. Johannessen, N.C. Nielsen, and M.H. Levitt, Chem. Phys. Lett. **242**, 304–309 (1995).

[40] M. Edén and M.H. Levitt, J. Chem. Phys. **111**, 1511–1519 (1999).

[41] A. Brinkmann and M.H. Levitt, J. Chem. Phys. **115**, 357–384 (2001).

[42] A. Brinkmann and A.P.M. Kentgens, J. Phys. Chem. B **110**, 16089–16101(2006).

[43] F.-C. Chou, S.-J. Huang, and J.C.C. Chan, J. Magn. Reson. **197**, 96–99 (2009).

[44] L. Chen, Q. Wang, B. Hu, O. Lafon, J. Trébosc, F. Deng, and J.-P. Amoureux, Phys. Chem. Chem. Phys. **12**, 9395–9405 (2010).

[45] A. Brinkmann, M. Edén, and M.H. Levitt, J. Chem. Phys. **112**, 8539–8554 (2000).

[46] B. Stevensson and M. Edén, J. Magn. Reson. **181**, 162–176 (2006).

[47] S.K. Zaremba, Ann. Mat. Pur. Appl. 293–317 (1966).

[48] H. Conroy, J. Chem. Phys. **47**, 5307–5318 (1967).

[49] V.B. Cheng, H.H. Suzukawa, and M. Wolfsberg, J. Chem. Phys. **59**, 3992–3999 (1973).

[50] T. Vosegaard, Z. Tošner, and N.C. Nielsen, Encyclopedia of Magnetic Resonance (2010).

[51] N. Stock and W. Schnick, Z. Naturforsch. **52B**, 251–255 (1997).

[52] H. Jacobs and R. Nymwegen, Z. Anorg. Allg. Chem. **624**, 199–204 (1998).

[53] C.A. Majid and M.A. Hussain, Proc. Pak. Acad. Sci. **33**, 11–17 (1996).

[54] J.E. Tibballs and R.J. Nelmes, J. Phys. C: Solid State Phys. **15**, 849–853 (1982).

[55] P. Langan, S.A. Mason, D. Myles, and B.P. Schoenborn, Acta Crystallogr., Sect. B: Struct. Sci. **58**, 728–733 (2002).

[56] C.C. Wilson, D. Myles, M. Ghosh, L.N. Johnson, and W. Wang, New J. Chem. **29**, 1318–1322 (2005).

[57] G. Kresse and J. Hafner, Phys. Rev. B **47**, 558–561 (1993).

[58] G. Kresse and J. Hafner, Phys. Rev. B **49**, 1425–14269 (1994).

[59] G. Kresse and J. Furthmüller, Comput. Mater. Sci. **6**, 15–50 (1996).

[60] G. Kresse and J. Furthmüller, Phys. Rev. B **54**, 11169–11186 (1996).

[61] P.E. Blöchl, Phys. Rev. B **50**, 17953–17979 (1994).

[62] G. Kresse and D. Joubert, Phys. Rev. B **59**, 1758–1775 (1999).

[63] H.J. Monkhorst and J.D. Pack, Phys. Rev. B **13**, 5188–5192 (1976).

[64] J.P. Perdew, A. Ruzsinszky, G.I. Csonka, O.A. Vydrov, G.E. Scuseria, L.A. Constantin, X. Zhou, and K. Burke, Phys. Rev. Lett. **100**, 136406 (2008).

[65] M. Hohwy, H.J. Jakobsen, M. Edén, M.H. Levitt, and N.C. Nielsen, J. Chem. Phys. **108**, 2686–2694 (1998).

[66] J. Schmedt auf der Günne, J. Magn. Reson. **165**, 18–32 (2003).

[67] R.K. Harris, E.D. Becker, S.M. Cabral de Menezes, P. Granger, R.E. Hoffman, and K.W. Zilm, Pure Appl. Chem. **80**, 59–84 (2008).

[68] M.E. Rose, *Elementary Theory of Angular Momentum* (Dover Publications, New York, 1995).

[69] P. Kempgens, J. Hirschinger, K. Elbayed, J. Raya, P. Granger, and J. Rosé, J. Phys. Chem. **100**, 2045–2052 (1996).

[70] H.W. Spiess, NMR: Basic Princ. Prog. **15**, 55-214 (1978).

[71] I.N. Bronstein, K.A. Semendjajew, G. Musiol, and H. Mühlig, *Taschenbuch Der Mathematik*, 5th ed. (Harri Deutsch, 2008).

[72] P. Hodgkinson and L. Emsley, J. Magn. Reson. **139**, 46–59 (1999).

[73] V.I. Lebedev, USSR Comput. Math. Math. Phys. **16**, 10–24 (1976).

[74] V.I. Lebedev, USSR Comput. Math. Math. Phys. **15**, 44–51 (1975).

[75] V.I. Lebedev and A.L. Skorokhodov, Russian Acad. Sci. Dokl. Math. **45**, 587–592 (1992).

[76] E.R. Andrew, W.S. Hinshaw, M.G. Hutchins, and P.C. Canepa, Chem. Phys. Lett. **26**, 50–52 (1974).

[77] Q. Wang, X. Lu, O. Lafon, J. Trébosc, F. Deng, B. Hu, Q. Chen, and J.-P. Amoureux, Phys. Chem. Chem. Phys. **13**, 5967–5973 (2011).

[78] J. Schmedt auf der Günne, J. Magn. Reson. **180**, 186–196 (2006).

[79] F.D. Doty, J. Kulkarni, C. Turner, G. Entzminger, and A. Bielecki, J. Magn. Reson. **182**, 239–253 (2006).

[80] P. Tekely and M. Goldman, J. Magn. Reson. **148**, 135–141 (2001).

[81] K. Elbayed, B. Dillmann, J. Raya, M. Piotto, and F. Engelke, J. Magn. Reson. **174**, 2–26 (2005).

[82] J.L. Carolan, Chem. Phys. Lett. **12**, 389–391 (1971).

[83] C. Müller, W. Schajor, H. Zimmermann, and U. Haeberlen, J. Magn. Reson. **56**, 235–246 (1984).

[84] C.A. Michal, J.C. Wehman, and L.W. Jelinski, J. Magn. Reson. B **111**, 31–39 (1996).

[85] D.H. Brouwer and J.A. Ripmeester, J. Magn. Reson. **185**, 173–178 (2007).

[86] J. Vaara, J. Jokisaari, R.E. Wasylishen, and D.L. Bryce, Prog. Nucl. Magn. Reson. Spectrosc. **41**, 233–304 (2002).

[87] E. Breitmaier and W. Voelter, Carbon-13 NMR Spectroscopy: High-Resolution Methods and Applications in Organic Chemistry and Biochemistry, 3rd ed. (VCH Verlagsgesellschaft, 1987).

[88] E. Breitmaier, *Structure Elucidation by NMR in Organic Chemistry: A Practical Guide*, 3rd ed. (John Wiley & Sons, Ltd., Chichester, 2003).

[89] J. Weber, M. Seemann, and J. Schmedt auf der Günne, Solid State Nucl. Magn. Reson. **43-44**, 42–50 (2012).

[90] F.-C. Chou, H.-K. Lee, and J.C.C. Chan, J. Chem. Phys. **133**, 114503 (2010).

[91] H.W. Spiess, U. Haeberlen, and H. Zimmermann, J. Magn. Reson. **25**, 55–66 (1977).